

Assessing the Reliability of Wind Power Operations under a Changing Climate with a Non-Gaussian Distributional Adjustment

Jiachen Zhang

Department of Applied and Computational Mathematics and Statistics,
University of Notre Dame (USA)

and

Paola Crippa

Department of Civil and Environmental Engineering and Geoscience,
University of Notre Dame (USA)

and

Marc G. Genton

Statistics Program,

King Abdullah University of Science and Technology (Saudi Arabia)
and

Stefano Castruccio*

Department of Applied and Computational Mathematics and Statistics,
University of Notre Dame (USA)

January 15, 2023

*scastruc@nd.edu

Abstract

Facing increasing societal and economic pressure, many countries have established strategies to develop renewable energy portfolios, whose penetration in the market can alleviate the dependence on fossil fuels. In the case of wind, there is a fundamental question related to the resilience (and hence profitability) of future wind farms to a changing climate, given that current wind turbines have lifespans of up to thirty years. In this work we develop a new non-Gaussian method to adjust assimilated observational data to simulations and to estimate future wind, predicated on a trans-Gaussian transformation and a cluster-wise minimization of the Kullback–Leibler divergence. Future winds abundance will be determined for Saudi Arabia, a country with a recently established plan to develop a portfolio of up to 16 GW of wind energy. Further, we estimate the change in profits over future decades using additional high-resolution simulations, an improved method for vertical wind extrapolation and power curves from a collection of popular wind turbines. We find an overall increase in daily profit of \$273,000 for the wind energy market for the optimal locations for wind farming in the country.

Keywords: Bias correction; Kullback-Leibler divergence; Non-Gaussian process; Nonstationary model; Spatio-temporal model; Wind energy

1 Introduction

The vast evidence of the negative effects of fossil fuel emissions (24) calls for a major systemic change in current strategies to produce and distribute energy throughout the world. Societies worldwide are adapting by developing renewable alternatives to reduce dependence on fossil fuels and to align with the standards imposed by the Paris Agreement (28). Wind has been the natural resource with the largest share of power generation worldwide, with the United States and China being the two major leaders (39). In the United States, renewable energies, with wind energy being a major contributor, are predicted to surpass coal in terms of share of the energy market by the end of this decade. Similarly, while European countries have an overall smaller absolute installed capacity, the penetration of the energy in the national grid is in percentage considerable, with a peak of 42% in Denmark.

The wind energy sector is at its early stages in developing countries such as Saudi Arabia. Despite being one of the countries with the highest per capita energy consumption (52), the sixth largest consumer of oil worldwide (3) and the largest in the Gulf Cooperating Council (GCC) (22), the transition to renewable energy is very recent and almost exclusively focused on solar energy (23). Currently Saudi Arabia's contribution to the GCC's renewable energy portfolio amounts to 16% of the total capacity, with only 0.2% available for sharing, and only 2% generated from wind (22). As part of the recently outlined 'Vision 2030' plan (33), Saudi Arabia aims to generate 16 GW of wind energy (32), positioning the country as one of the major global wind energy suppliers and considerably contributing to the planned emissions reduction targets stipulated in the United Nations Framework Convention on Climate Change (47). Investments in wind energy would also result in the increased reliability of renewable energy, as for example solar energy is only available during daytime, whereas winds often peak at nighttime.

Under the aforementioned scenario, a comprehensive analysis must be conducted to

identify optimal sites for developing windfarms based on a cost-benefit analysis. Several recent studies with global climate models at annual (25) and monthly (26) scale, and later at daily level (42; 44), including validation of observational and simulated data sets (6) and extreme wind conditions (7), provided initial evidence about the availability of sufficient wind for installing wind turbines. Very recently, (14) conducted the first full feasibility study with a new high-resolution ensemble and identified the optimal locations and types of turbine based on maintenance and operational costs. While their study provided the first detailed assessment of the country’s resources, it relied on only four years of data, from 2013 to 2016, due to computational and storage constraints. This timescale is inconsistent with the current lifespan of wind turbines, which can be as long as thirty years, and the multidecadal effects of climate change could have an impact on the wind resource availability.

In order to provide a pathway for a feasible and robust implementation of a wind energy portfolio, the question of resilience under a changing climate must be addressed. Given the computational impossibility to simulate high resolution numerical simulations for decades, an alternative strategy focused on publicly available data must be devised. In this work we focus on developing a methodology for assessing future winds, predicated upon the estimation of the relationship between simulated and observed data for a historical period at the same spatial and temporal scales. Under the assumption of an enduring relation between these two data sets, future wind behaviors are estimated by applying the same relation to future climate simulations.

Methods for adjusting observations and simulations have a long history in geoscience (see, e.g., (54; 27) and (21; 17) for a general review). In its simplest form, the bias correction method focuses on an individual time series, estimates the differences between observational and simulated historical climate, and applies this difference to future simulations to obtain the future observations. Slightly more sophisticated approaches involve also the use of

variance (see Section 3 for a comprehensive review). With the exception of some studies (e.g., (36; 50)), the vast majority of literature has focused on the adjustment of first and second moments for the marginal distribution of a time series.

Only recently statistical methodologies focused on adjustments of the joint spatial or temporal distribution have been proposed. (30) proposed a spectral-based approach to the adjustment of time series, thus resulting in an adjustment of the implied covariance structure. At the core of this method, formulated as a generalization of the ‘Delta method’ (17), is the notion of (penalized) estimation of the ratio between the spectral densities of observations and simulations. (37) proposed a generalization of the aforementioned approach to a transient climate and multiple simulations under different future scenarios. In this work, we propose a new approach based on a non-Gaussian clusterwise spatial transformation, which is estimated by minimizing the distance between the joint distribution of the observational and of the simulated data field. Our proposed approach is based on three fundamental ideas: 1) non-Gaussianity can be accounted for through a marginal transformation which is slowly varying in space; 2) the transformation to Gaussianity can be inferred by minimizing the distributional distance between the two fields, as long as this value is comparable, and possibly within the confidence interval of the maximum likelihood estimate; and 3) transformation to Gaussianity allows a simple adjustment of first and second moments and a back-transformation to the original scale. Besides the obvious difference of being focused on space rather than time, our proposed method approaches the adjustment of the joint distribution under a different perspective from (30) and (37), as it explicitly aims to transform the data to Gaussianity instead of adjusting its spectral representation. While their proposed method incidentally ‘retained most non-Gaussian characteristics of data’, this was not the primary objective, while in this work a transformation/back-transformation to non-Gaussianity ensures the preservation of the marginal distribution.

Section 2 introduces the data sets used for this study, validates the historical wind

speeds across Saudi Arabia, and proposes a model for the mean and temporal dependence. Section 3 reviews current approaches to observation-simulation corrections. Section 4 introduces the proposed methodology for non-Gaussian adjustment. Section 5 validates the model with a simulation study with non-Gaussian random fields and historical data. Section 6 applies the proposed methodology, along with vertical wind extrapolation and power curve evaluation, to estimate the change in daily profits from future winds in Saudi Arabia. Section 7 concludes with a discussion. The code for this manuscript is available at github.com/jiachenzhang001/Non-Gaussian-Bias-Correction the following GitHub repository: github.com/jiachenzhang001/Non-Gaussian-Bias-Correction.

2 Data and preprocessing

In this study, we focus on daily wind speed data at 10 meters above the ground level in Saudi Arabia, which is bounded approximately by longitudes of $34^{\circ}E$ – $56^{\circ}E$ and latitudes of $16^{\circ}N$ – $33^{\circ}N$ (see Figure 1(a-b)). Wind speed is derived as the Euclidean norm from the zonal and meridional velocity (i.e., over the x and y axes). We present the data set of the power curves along with the information related to the cost of energy in the supplementary material.

2.1 Observational data

We use the Modern-Era Retrospective Analysis for Research and Applications, version 2 (MERRA-2, (13)), available from 1980 to the present day. Reanalysis data consists of observational data assimilated to a numerical weather model and, in the geoscience community, this data product is considered the best representation of the state of the Earth’s system. MERRA-2 is the reference observational data set used in our study and is available on a regular grid with a resolution of $0.625^{\circ} \times 0.5^{\circ}$ in longitude and latitude,

respectively. We only use daily wind speed data from 1980 to 2005, for a total of 26 years, to match the simulation data sets presented in Section 2.2. There are $n = 614$ locations in Saudi Arabia at MERRA-2 resolution for a total of $T = 9,497$ days. Throughout this manuscript, we will denote the MERRA-2 wind fields as $W_O(\mathbf{s}_i, t_j)$, where the subscript O indicates the observation.

2.2 Regional simulations

We use the simulations from the Coordinated Regional Climate Downscaling Experiment (CORDEX), which is a set of coordinated regional experiments. Specifically, we focus on the Middle East North Africa (MENA) CORDEX Program, and among the five available simulations, we select CORDEX-4, which exhibits the best agreement with MERRA-2 in Saudi Arabia, as demonstrated by (6). The simulation resolution is $0.22^\circ \times 0.22^\circ$, finer than MERRA-2, and boundary conditions for the historical and future periods are provided by the Geophysical Fluid Dynamics Laboratory global coupled climate-carbon Earth System Models (GFDL-ESM2M, (9)). Future GFDL-ESM2M runs are simulated under the Representative Concentration Pathways 8.5 (RCP 8.5, (48)) scenario, in which the global radiative forcing is assumed to increase by 8.5 W/m^2 by 2100 (45). We regrid and upscale the MENA CORDEX data to the MERRA-2 resolution by considering the average of locations in MENA CORDEX that are within the range of two consecutive MERRA-2 grids. Even though the historical run spans from 1950 to 2005, we only consider data from 1980 to 2005 to align the observation window with MERRA-2; for future runs we only consider simulations in the near future for the same number of years, i.e., from 2025 to 2050. We will denote the MENA-CORDEX wind fields as $W_S(\mathbf{s}_i, t_j)$, where the subscript S indicates for simulation.

2.3 Overview of the MENA CORDEX and MERRA-2 representation of wind fields in Saudi Arabia

Figure 1(a-b) show the average daily wind speed from year 1980 to 2005 from MENA CORDEX and MERRA-2, respectively, during June, July, and August, which correspond to the season with the highest winds (6; 14). Wind from MENA CORDEX is consistently lower than from MERRA-2, which is apparent when comparing the color scales of the two maps. Moreover, both panels show that the average wind speed is high near the water masses of the Red Sea, Mediterranean and Persian Gulf due to strong temperature and pressure gradients between land and ocean. MERRA-2 also indicates strong winds towards the central plateau where the capital Riyadh is located.

Figure 1(c) compares the spatially averaged annual cycle. Despite a strong additive bias, MENA CORDEX and MERRA-2 agree in terms of the annual cycle, the wind speed is at its highest and lowest during summer and winter, respectively. This annual variability is attributable to Saudi Arabia's location within the trade-wind belt (Hadley cell) of the Northern Hemisphere (16). During winter, wind travels south from the Mediterranean to the Persian Gulf. However, with the advent of spring, the northern wind becomes stronger, and the monsoon season brings southeastern wind from the Indian Ocean to the southeastern part of the peninsula and the Arabian Sea. Figure 1(d) shows the Taylor diagram, a standard graphical diagnostics in polar coordinates between two data sets, with the radius representing the ratio of standard deviations and the angle being proportional to the correlation between the two data sets. The diagram compares data aggregated at daily and monthly level. Unsurprisingly, the two data sets are more strongly correlated at monthly level, and the variability of MENA CORDEX is smaller (larger) at daily (monthly) level when compared to that of MERRA-2. Further comparison is shown in Figure S1 of the supplementary materials.

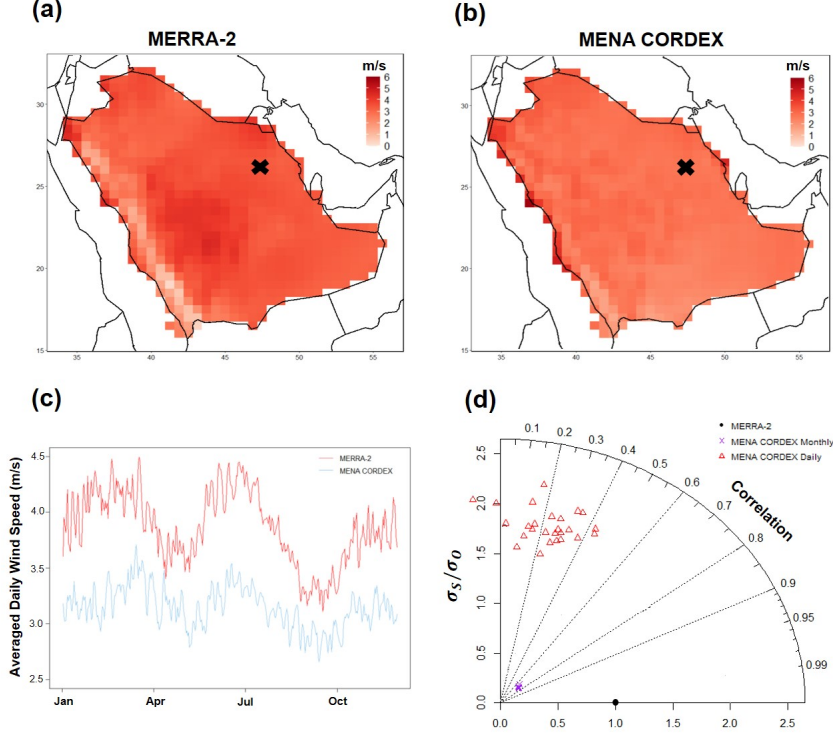


Figure 1: Average daily wind speeds for June-July-August from 1980 to 2005 for (a) MERRA-2 and (b) MENA CORDEX; (c) Annual cycle of daily wind speed in Saudi Arabia from MENA CORDEX and MERRA-2; (d) Taylor diagram of monthly (purple crosses), and daily (red triangles) wind speeds from MENA CORDEX, and MERRA-2 (black dot). σ_0 and σ_s are the spatial standard deviations of MERRA-2 and MENA CORDEX, respectively.

2.4 Model for the mean and temporal dependence

We assume a periodic climatology described by K harmonics in order to account for the inter-annual wind variability. If we denote the wind speed for location s and time t by

$W(\mathbf{s}, t)$, its interannual variability across the year can be written as

$$\begin{aligned} W(\mathbf{s}_i, t_j) &= \mu(\mathbf{s}_i, t_j) + \sum_{i'=1}^P \phi_{i',i} \varepsilon(\mathbf{s}_i, t_{j-i'}) + \varepsilon(\mathbf{s}_i, t_j), \\ \mu(\mathbf{s}_i, t_j) &= \omega_i * \text{yr}(t_j) + \sum_{k=1}^K \left\{ \beta_{k,i} \sin\left(\frac{2\pi k t_j}{\delta}\right) + \beta'_{k,i} \cos\left(\frac{2\pi k t_j}{\delta}\right) \right\}, \end{aligned} \quad (1)$$

where $\delta \in \{365, 366\}$ depending on whether the year is non-leap or leap, $\mathbf{s}_i = (x_i, y_i)$, $i = 1, \dots, n$; $j = 1, \dots, T$, and $\text{yr}(t)$ represents the year of day t . Thus, the model assumes a location-specific linear annual trend, with K harmonics to explain inter-annual variability and P autoregressive coefficients. We further assume that $\varepsilon(\mathbf{s}_i, t_j)$ is independent across t_j with a spatial dependence that will be specified later. The mean and the autoregressive coefficients are estimated through site-specific inference, initially by assuming Gaussian errors and independence in time for estimating $\{\omega_i, \beta_{k,i}, \beta'_{k,i}\}$ and subsequently estimating ϕ_i by maximum likelihood. In the supplementary material we present diagnostics to show that 1) the linear trend ω_i is significant for the majority of points in both data sets (Figure S2); 2) two harmonics ($K = 2$) are sufficient to explain the climatology for both data sets (Figure S3); 3) the parameters $\beta_{k,i}, \beta'_{k,i}, \phi_i$ are constant in time (Figures S4 and S5); and 4) the residuals of (1) are uncorrelated in time (Figure S6).

3 Review of adjustment approaches

MERRA-2 represents the state of the system assimilated from observations, so it can be observed up to the present and its future needs to be estimated. The simulations obtained from MENA CORDEX can be used as a proxy to assess the future wind speed. From the preliminary analysis in Section 2.3, a systematic mismatch between the two data sets is apparent. The objective of this study is to provide an adjustment of this mismatch in the historical period and use it to predict future MERRA-2 observations using the available future MENA CORDEX simulations. While the methods are general, for consistency with

the previous section, we will denote the spatio-temporal wind fields as $\mathbf{W}_O^{(H)}$ and $\mathbf{W}_S^{(H)}$ for MERRA-2 (O for observations) and MENA CORDEX (S for simulations), respectively, for the historical period (1980-2005). The future data will be denoted as $\mathbf{W}_O^{(F)}$ and $\mathbf{W}_S^{(F)}$. Throughout this section, we will refer to MERRA-2 as ‘observations’ and MENA CORDEX as ‘simulations’ to emphasize the generality of our methodology.

3.1 Correction for marginal distributions

The simplest approach to achieve adjusted future simulations is bias correction, which assumes a simple additive bias between observations and simulations, estimates it in the historical period, and then adjusts future simulations. Bias correction has been widely used in a number of studies in geoscience (see, e.g., (18; 5) for wind applications). This approach assumes that there is no difference in marginal variance, spatial covariance, or other high-order moments. Formally, we assume that the observation-corrected data for a location \mathbf{s}_i can be expressed as

$$W_O^{(F)}(\mathbf{s}_i, t_j) = W_S^{(F)}(\mathbf{s}_i, t_j) + \left\{ \mu_O^{(H)}(\mathbf{s}_i, t_j) - \mu_S^{(H)}(\mathbf{s}_i, t_j) \right\}, \quad (2)$$

where t_j refers to the j th time for the historical or future time period, and $\mu_\ell^{(H)}(\mathbf{s}_i)$ for $\ell = \{O, S\}$ is the mean in the historical period (from 1980 to 2005), which is estimated via the location-specific inference of the mean parameters in (1), as described in Section 2.

Two data sets typically exhibit differences also in their temporal variability (see Figure S1), which cannot be accounted for by a simple bias correction. Therefore, a relatively more articulated approach focuses on adjusting both the mean and variance (46; 31). Formally:

$$W_O^{(F)}(\mathbf{s}_i, t_j) = W_S^{(F)}(\mathbf{s}_i, t_j) + \frac{\sigma_O^{(H)}(\mathbf{s}_i)}{\sigma_S^{(H)}(\mathbf{s}_i)} \left\{ \mu_O^{(H)}(\mathbf{s}_i, t_j) - \mu_S^{(H)}(\mathbf{s}_i, t_j) \right\}, \quad (3)$$

where $\sigma_\ell^{(H)}(\mathbf{s}_i)$ for $\ell = \{O, S\}$ is the standard deviation in the historical period, and is estimated from the parameters of the autoregressive process in (1).

3.2 Covariance adjustment

In the previous section, the adjustment was performed independently for every grid point, hence focusing only on the marginal distribution, without considering the potential dependence across multiple locations. However, there is strong evidence of spatial dependence in the observed and simulated field. Indeed, Figure S8 indicates a strong empirical spatial correlation between two neighboring points for both data sets. It is therefore of interest to develop methods to correct not just for the mean and variance, but also for the spatial correlation.

Under the assumption of Gaussianity, a simple generalization of (3) allows for adjustment of both the mean and covariance matrix (therefore including variance). Indeed, future observations can be expressed as:

$$\mathbf{W}_O^{(F)}(t_j) = \mathbf{W}_S^{(F)}(t_j) + (\boldsymbol{\Sigma}_O^{(H)})^{\frac{1}{2}} \left\{ (\boldsymbol{\Sigma}_S^{(H)})^{-\frac{1}{2}} \right\}^\top \left\{ \boldsymbol{\mu}_O^{(H)}(t_j) - \boldsymbol{\mu}_S^{(H)}(t_j) \right\}, \quad (4)$$

where $\boldsymbol{\mu}_\ell^{(H)}(t_j) = (\mu_k^{(H)}(\mathbf{s}_1, t_j), \dots, \mu_k^{(H)}(\mathbf{s}_n, t_j))$ (with the same convention being used for the other quantities), and $\boldsymbol{\Sigma}_\ell^{(H)}$ for $\ell = \{O, S\}$ denotes the covariance matrices for the observational and simulated data sets in the historical period, and the superscript $\frac{1}{2}$ denotes the Cholesky decomposition. While $\boldsymbol{\Sigma}_\ell^{(H)}$ could be estimated using a simple nonparametric sample covariance matrix, the relatively large number of locations ($n = 614$) would result in an unstable estimate. Instead, we assume spatial dependence via two parametric models in increasing order of complexity. First, we consider a stationary and isotropic covariance function modeled by the Matérn correlation (41), i.e., if two measurement are separated by distance h , then their correlation is

$$C(h) = \frac{2^{1-\nu}}{\Gamma(\nu)} \left(\sqrt{2\nu} \frac{h}{\rho} \right)^\nu K_\nu \left(\sqrt{2\nu} \frac{h}{\rho} \right), \quad (5)$$

where $\rho > 0$ is the range parameter, $\nu > 0$ is the smoothness of the process, and K_ν is the Bessel function of the second kind of order ν . Second, we consider a more articulated

nonstationary covariance resulting from the kernel convolution representation of the random field (20), which can be written in closed form under a general class of kernels as (34)

$$C(\mathbf{s}, \mathbf{s}') = \sigma(\mathbf{s})\sigma(\mathbf{s}') \frac{|\Sigma(\mathbf{s})|^{1/4}|\Sigma(\mathbf{s}')|^{1/4}}{\left|\frac{\Sigma(\mathbf{s}) + \Sigma(\mathbf{s}')}{2}\right|^{1/2}} g\left(\sqrt{Q(\mathbf{s}, \mathbf{s}')}\right), \quad (6)$$

where

$$Q(\mathbf{s}, \mathbf{s}') = (\mathbf{s} - \mathbf{s}')^\top \left(\frac{\Sigma(\mathbf{s}) + \Sigma(\mathbf{s}')}{2}\right)^{-1} (\mathbf{s} - \mathbf{s}').$$

In this study, the function g is specified to be the exponential function (although several other alternatives are possible) with a spatially varying range. All the spatially varying parameters are defined through the mixture of fixed knots for A fixed locations $\mathbf{b}_a, a = 1, \dots, A$. Herein, we select $A = 4$ as a larger number of knots would imply a considerable increase in computational cost. The spatially varying variance is defined as

$$\sigma(\mathbf{s}) = \sum_{a=1}^A w_a(\mathbf{s})\sigma_a, \quad w_a(\mathbf{s}) \propto \exp\left\{-\frac{\|\mathbf{s} - \mathbf{b}_a\|^2}{2\lambda_\sigma}\right\},$$

where the weights are normalized and λ_σ could be estimated, but for simplicity it is here assumed to be fixed at one half of the minimum distance between the knots. A similar approach is used to define $\Sigma(\mathbf{s})$ and the exponential function range. Inference is performed through local likelihood, see (40) for details.

4 Adjusting for non-Gaussian spatial data

The methods presented in Section 3 allow to correct the joint distribution under the assumption that the mean and covariance are the only quantities for which the adjustment is necessary. This is appropriate only for physical variables whose temporal aggregation is sufficiently large to ensure at least approximate Gaussianity. Wind data aggregated at daily or subdaily level are generally expected to exhibit non-Gaussian behaviors, and in

particular, to be skewed to the right owing to occasionally high values because of local meteorological events such as storm fronts or persistent wind gusts. This is indeed the case in our application. Figure 2(a) shows the histogram of the MENA CORDEX data from a location at the northwest end of Saudi Arabia represented by a cross in Figure 1(a-b). The superimposed best fit for a Gaussian distribution is vastly inadequate as it fails to capture the aforementioned right skew. Furthermore, the red boxplots in Figure 2(c-d) show the skewness and excess kurtosis for all locations in MENA CORDEX, with a characteristic right skew and some degree of excess kurtosis.

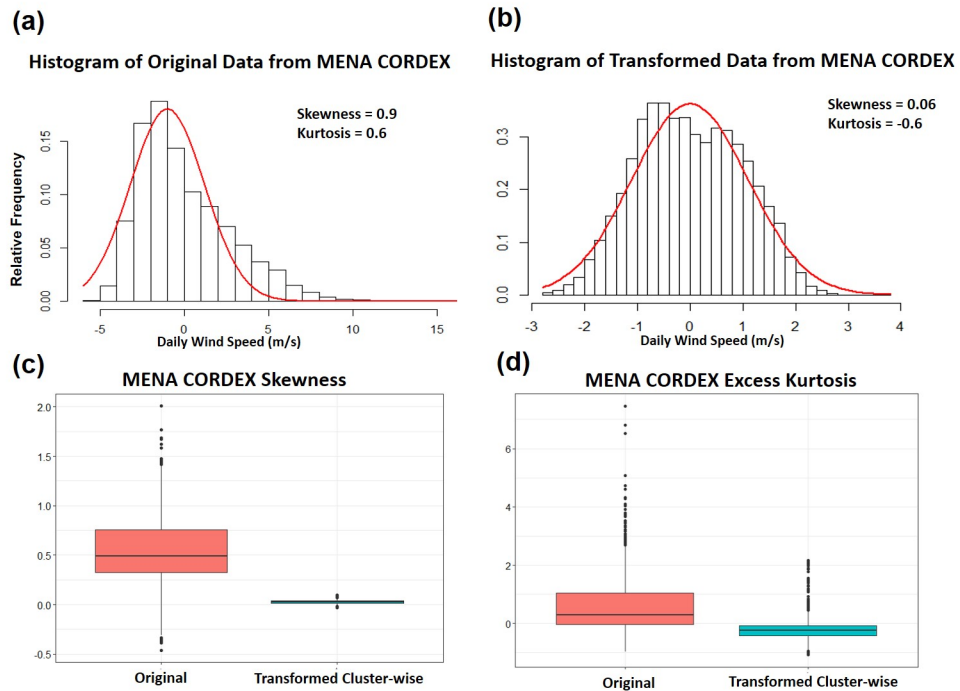


Figure 2: Comparison of the MENA CORDEX data from 1980 to 2005 before and after transformation. Histogram of the (a) original and (b) transformed data at one selected location (see the cross in Figure 1(a-b)). The red line represents the Normal distribution that best fits the data. Boxplot of (c) skewness and (d) excess kurtosis at all locations.

We propose a correction method for non-Gaussian data based on marginal, spatially varying transformations. We denote this transformation to Gaussianity by g_λ , a function depending on λ , and we assume the same class of transformation by g_λ with $\lambda = (\lambda_1, \dots, \lambda_n)^\top$ indicating the element-wise transformation at each location. Future observations are then obtained as

$$\mathbf{W}_O^{(F)}(t_j) = g_{\lambda_O}^{-1} \left[g_{\lambda_S}(\mathbf{W}_S^{(F)})(t_j) + (\Sigma_O^{(H)})^{\frac{1}{2}} \left\{ (\Sigma_S^{(H)})^{-\frac{1}{2}} \right\}^\top \left\{ \mu_O^{(H)}(t_j) - \mu_S^{(H)}(t_j) \right\} \right], \quad (7)$$

where now $\mu_\ell^{(H)}(\mathbf{s}_i)$ and $\Sigma_\ell^{(H)}$ for $\ell = \{O, S\}$ represent the mean and covariance matrix of the *transformed* process $g_{\lambda_\ell}(\mathbf{W}_\ell^{(H)})(t_j)$, respectively. In the next sections, we will discuss the particular choice of transformation g_λ and the assumptions on λ to allow an approximately optimal choice across the entire spatial domain.

4.1 The Yeo-Johnson transformation

The standard Box-Cox transformation (11) cannot be used for g_λ , as our objective is to transform residuals, which are not necessarily non-negative. Instead, we rely on a similar function, the Yeo-Johnson transformation (53):

$$g_\lambda(x) = \begin{cases} [(x+1)^\lambda - 1]/\lambda, & x \geq 0, \lambda \neq 0, \\ \log(x+1), & x \geq 0, \lambda = 0, \\ -[(-x+1)^{2-\lambda} - 1]/(2-\lambda), & x < 0, \lambda \neq 2, \\ -\log(-x+1), & x < 0, \lambda = 2. \end{cases}$$

While the standard approach for estimating λ is to maximize the likelihood of transforming the data to Gaussianity, our objective is to minimize the (joint) distributional distance, which in this work is measured as the Kullback-Leibler divergence (KL divergence (29), see Section 4.2), between the observational and simulated data. The key idea of our proposed approach is that even if the parameter is estimated by minimization of KL

divergence and not Maximum Likelihood Estimator (MLE), their difference is not substantial. Indeed, for a sizable number of sites the (asymptotic, likelihood based) 95% confidence interval for the MLE includes the parameter obtained via distance minimization, despite its narrow range owing to the sample size from $T = 9,497$ days (see Figure S9). Once the parameter has been inferred for both data sets and the transformation has been applied, the bias and covariance from the correction method in Section 3.2 are estimated under the assumption of Gaussianity, and the results are applied to the future simulated data to obtain an estimate for future observational data as explained in equation (7). As an example, Figure 2(b) shows the result for the transformed wind field according to the method proposed in this study for one location, resulting in an approximately Gaussian distribution. Figure 2(c-d) show the skewness and excess kurtosis at all the locations before and after the transformation (with MLE, see Figure S10 for the results with KL divergence), and it is readily apparent how the transformation is sufficiently flexible to transform the data to Gaussianity at all locations.

4.2 *k*-Nearest Neighbors Approximation of the Kullback-Leibler Divergence

The KL divergence is a measure of how one probability distribution differs from a second reference probability distribution. In this study, we estimate the KL divergence between the simulations and observations, denoted as f_S and f_O respectively:

$$D_{KL}(f_O||f_S) = \int f_O(x) \log \left\{ \frac{f_O(x)}{f_S(x)} \right\} dx. \quad (8)$$

In our case, a direct evaluation is computationally impossible as comparing two multivariate distributions of dimension $n = 614$ would require an integration over the same number of dimension in (8). While a simplifying expression is available for the Gaussian distribution, it will not be used here as a comparison with different methods in the original non-Gaussian

scale must be made. Therefore, we rely upon a numerical approximation of the integral using k -nearest-neighbor (k -NN) (31; 51). Let us assume that we have two n -dimensional random samples from two populations with probability density functions f_O and f_S . We define the distance between the i th sample from f_O and 1) its k -NN in the same population as $\rho_{k'}(i)$, and 2) its k -NN in the other population as $\nu_{k'}(i)$. Then, we use the following approximation (51):

$$\hat{D}_{KL}(f_O||f_S) = \frac{1}{n} \sum_{i=1}^n \log \frac{\hat{f}_O(\mathbf{X}_i)}{\hat{f}_S(\mathbf{X}_i)} = \frac{n}{m} \sum_{i=1}^m \log \frac{\nu_{k'}(i)}{\rho_{k'}(i)} + \log \frac{m'}{m-1}, \quad (9)$$

where $\hat{f}_O^{(k')}(X_i) = \frac{k'}{m-1} \cdot \frac{1}{v_1(n)\rho_{k'}^{d'}(i)}$ and $\hat{f}_S^{(k')}(X_i) = \frac{k'}{m'} \cdot \frac{1}{v_1(d)\nu_{k'}^{d'}(i)}$ are the k -NN estimators of f_O and f_S , respectively, $v_1(n) = \frac{\pi^{n/2}}{\Gamma(\frac{n}{2}+1)}$, and $\Gamma(\cdot)$ is the Gamma function.

In our case, the dimension is equal to the number of locations, i.e. $n = 614$, and the number of samples $m = m' = 4,749$ (13 years of data in the testing set, as detailed in Section 2) since we evaluated MENA CORDEX and MERRA-2 for the same time period. One critical aspect of this approximation is the selection of k' , i.e., the number of nearest neighbors. In this study, the standard convention of using the square root of the number of observations is used (2), so that $k' = \sqrt{4,749} \approx 70$.

4.3 K-means Clustering

To determine the transformation in (7), λ_O and λ_S must be estimated. While it is possible in principle to estimate all $2n = 1,222$ location-specific parameters jointly, this would lead to an unnecessary and severe overparametrization, as geographically close locations are expected to have similar estimates. In practice, a joint estimation is also computationally infeasible, since it would require a simultaneous optimization over all $2n$ parameters.

In order to reduce the parameter space, and consequently the computational time, we assume that λ_O and λ_S are constant across some regions with a k -means clustering

approach, i.e., for some p -variate observations $\mathbf{x}_1, \dots, \mathbf{x}_n$ and a fixed k'' , we aim to minimize the distance between elements of each cluster and its mean.

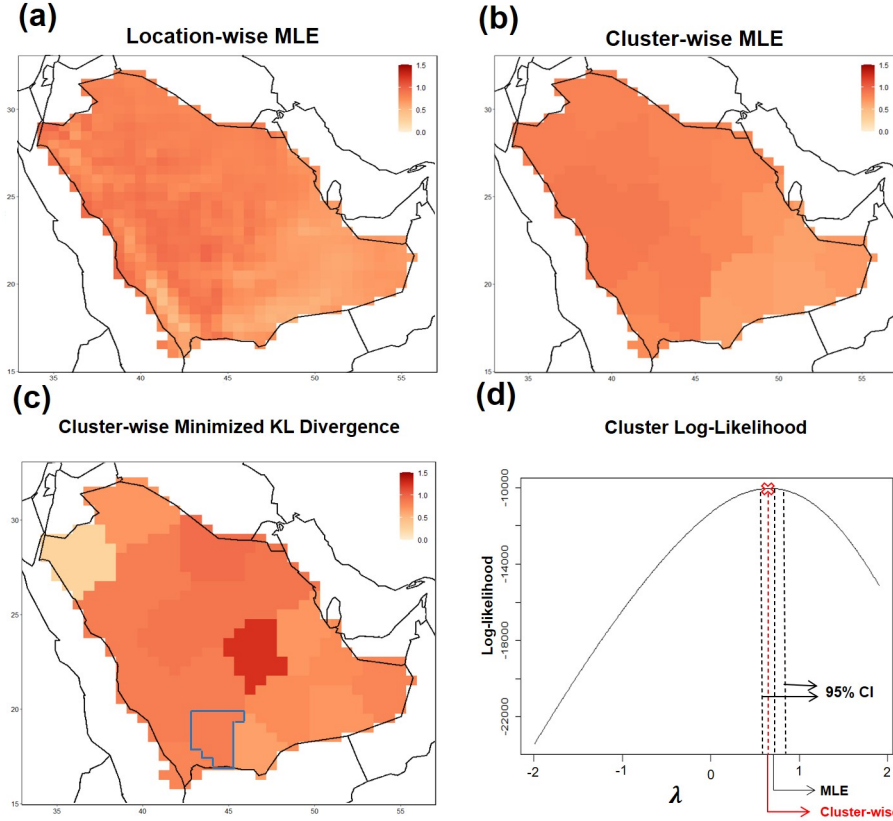


Figure 3: MENA CORDEX maps of (a) the Yeo-Johnson MLE; (b) the cluster-wise MLE and (c) the cluster-wise parameter estimated by minimizing the KL divergence. (d) The log-likelihood profile of the cluster indicated in (c), the red cross represents the cluster-wise parameter, and the outer-most dashed lines indicate the 95% confidence interval of the MLE.

While our main interest is to obtain regions with similar $\boldsymbol{\lambda}_O$, it would be desirable to have spatially coherent clusters for interpretability. Therefore, we assume that for each site, we have $p = 3$ covariates: the MLE of the element of $\boldsymbol{\lambda}_O$ corresponding to that site, the

latitude, and the longitude. Preliminary exploratory analysis (not shown) indicates that a weighted version of k -means with even a small weight on latitude and longitude allows for spatially coherent clusters. Therefore, we will assume a weight of 0.98 on the MLE and a weight of 0.01 each for the latitude and longitude, and $k'' = 20$ clusters, each with thirty to fifty grids, as shown in Figure 3(b-c). The usage of clusters instead of location-specific parameters implies some loss of information. For MENA CORDEX, Figure 3(a) shows the map of the pointwise MLEs (see Figure S9(a) for MERRA-2), whereas Figure 3(b) shows the clusterwise MLEs. Both the values and spatial patterns are visually similar. Figure S9(b-c) show the map of the points whose (asymptotic, likelihood-based) confidence interval for pointwise MLEs include the MLE for the corresponding cluster of both data sets. Despite the very small intervals resulting from $T = 9,497$ observations, a sizable portion of the sites (50% MERRA-2 and 37% for MENA CORDEX) includes the cluster MLE.

Even though our objective is to estimate $\boldsymbol{\lambda}_\ell = (\lambda_{\ell;1}, \dots, \lambda_{\ell;k''})^\top, \ell = \{O, S\}$ (i.e., the parameters for each cluster) such that the KL divergence is minimized, the resulting value must not be too different from the MLE to still achieve Gaussianity. Figures 3(b) and 3(c) compare the cluster-wise MLE and KL minimizer for MENA CORDEX. Their patterns are very similar, albeit with a few noticeable differences. 12 clusters from among $k'' = 20$ have the KL minimizer inside the MLE confidence interval for both MENA CORDEX and MERRA-2, and Figure 3(d) shows an example of the cluster highlighted in the southern part of the country. In the case of pointwise MLEs, despite the narrow interval from the large number of observed days, the KL minimizers in panel (c) fall within the interval from panel (b).

5 Validation with simulations and real data

In this section, we validate our proposed methodology with respect to traditional approaches in terms of the KL divergence for 1) two simulated non-Gaussian random fields, and 2) the MENA CORDEX simulations and MERRA-2 data. Throughout this section, we use M to denote the marginal bias correction with mean (2), MV to denote mean and variance (3), MC and MN to denote the mean and covariance in model (4) via the Matérn parameters in (5) and the nonstationary model (6), respectively. Further, we compare these methods with our proposed approach in (7) for two cases in which the nonstationary covariance (6) is used. In the first case, denoted as $T1$, a single transformation parameter is considered for each of the observations and simulations, so that all locations are transformed by the same parameter, minimizing the KL divergence. In the second case denoted as TC , we use a cluster-wise parameter determined by k -means as specified in Section 4.3, for each of the two data sets. Thus, the locations in the same cluster are transformed by the same parameter and the vector of all cluster transformations minimizes the KL divergence across all the sites. Computational details are presented in the supplementary material.

5.1 Simulated data

We perform a simulation study to assess the model performance in capturing varying degrees of non-Gaussianity. Both data sets are simulated from two random fields that cannot be transformed to Gaussianity with a simple marginal transformation. Furthermore, to simplify the setting, we do not assume any inter-annual or annual trend or temporal dependence (i.e., $\phi_{i',i} = \beta_{k,i} = \beta'_{k,i} = \omega_i = 0$ for all $i = 1, \dots, n, i' = 1, \dots, P$, and $k = 1, \dots, K$ in (1)). The spatial domain of our simulation comprises of 200 locations divided into $R = 8$ spatial regions with 25 points each on a 5×5 grid in a square of length 1. For each simulation, 100 replicates were generated, among which the first 50 were

considered the historical period, and the last 50 were considered the future period. A total of 1,000 simulations was performed.

As ‘observational’ data, we simulated samples from a bi-resolution model with a non-Gaussian marginal distribution (44; 43). For each region $r = 1, \dots, R$ we have

$$W_O^{(\ell)}(\mathbf{s}) = \frac{\lambda^{\text{SKT}} |U_r^{\text{SKT}}| + \eta_r^{\text{SKT}}(\mathbf{s})}{\sqrt{Z_r^{\text{SKT}}}}, \quad (10)$$

where $\ell = \{H, F\}$, and the temporal index has been omitted for simplicity, $Z_r^{\text{SKT}} \sim \text{Gamma}(\nu^{\text{SKT}}/2, \nu^{\text{SKT}}/2)$ independent and identically distributed, and $\mathbf{U}^{\text{SKT}} = (U_1^{\text{SKT}}, \dots, U_R^{\text{SKT}})^\top \sim \mathcal{N}(\mathbf{0}, \Sigma_0^{\text{SKT}})$ and $\eta_r^{\text{SKT}}(\mathbf{s})$ indicate a zero mean Gaussian random field independent across r with covariance matrix Σ_r^{SKT} . The model assumes that, for each region r , the two effects Z_r^{SKT} and U_r^{SKT} are constant, and the small scale variation is accounted by the field $\eta_r^{\text{SKT}}(\mathbf{s})$. Across the regions, the vector \mathbf{U}^{SKT} characterizes the large scale dependence. This model (10) exhibits a skew- t marginal distribution, i.e., a perturbation of the t distribution accounting for skewed behavior (1) and it can be represented hierarchically, thereby allowing relatively fast frequentist or Bayesian inference. For our simulation, we fix the parameters $\lambda^{\text{SKT}} = 0.8$ and $\nu^{\text{SKT}} = 8$ and assume that Σ_r^{SKT} and Σ_0^{SKT} are generated from exponential covariance functions with ranges of 0.2 and 0.5, respectively, corresponding to maximum correlations of 0.77 and 0.24, respectively. The large correlation within each region is in accordance with the previous results with bi-resolution models, where the majority of the dependence is explained by the small scale (4; 44). Additional simulations with parameter choices leading to weaker and stronger correlation are shown in Figure S11.

The ‘simulation’ data are obtained from a Gaussian-Log-Gaussian (GLG, (35)), which assumes

$$W_S^{(\ell)}(\mathbf{s}) = \frac{\eta^{\text{GLG}}(\mathbf{s})}{\sqrt{\xi^{\text{GLG}}(\mathbf{s})}} + \varepsilon^{\text{GLG}}(\mathbf{s}), \quad (11)$$

where $\ell = \{H, F\}$ and $\eta^{\text{GLG}}(\mathbf{s})$ is an isotropic zero mean Gaussian field with covariance

function C^{GLG} , which is considered to be an exponential with a range parameter of 0.2. The process $\xi^{\text{GLG}}(\mathbf{s})$ is such that $\log\{\xi^{\text{GLG}}(\mathbf{s})\}$ is a Gaussian field with mean $-\nu^{\text{GLG}}/2$ and covariance function $\nu^{\text{GLG}}C^{\text{GLG}}$, where C^{GLG} is exponential with a range of 0.7, so that marginally $\xi^{\text{GLG}}(\mathbf{s})$ is lognormal with mean 1 and variance $\exp(\nu^{\text{GLG}}) - 1$, and $\nu^{\text{GLG}} = 8$ in our simulation. The error term $\varepsilon^{\text{GLG}}(\mathbf{s})$ represents an independent Gaussian noise with zero mean and variance $\tau^2;^{\text{GLG}} = 0.1$, representing the micro-scale variability or the nugget effect. As for the bi-resolution model (10), model (11) cannot be transformed to Gaussianity with a simple marginal transformation; thus our proposed approach is not trained to obtain an exact transformation to Gaussianity for either the ‘observed’ or ‘simulated’ data sets.

Figure 4(a) shows the results in terms of the KL divergence ratio between the MV method and MC, MN, T1, and TC (M is not applied because the ‘simulated’ data have zero mean by construction), where each element of the boxplots represents one of the 1,000 simulations. Despite the considerably different and non-trivial non-Gaussian structures of the two data sets, the proposed approach can more closely estimate the true future observations against a Gaussian transformation, with an improvement of 29% in the median using a single transformation in T1. The clusterwise transformation TC yields a further improvement of 31%, although at an increased computational cost, because the transformation parameters must be separately estimated for each region.

5.2 Wind speed data

Since future observations cannot be used to validate our model, we only consider the historical data period, and we separated it into a training and testing set. We use the first thirteen years of data (1980 to 1992) as the training set and the last thirteen years (1993 to 2005) as the test set. Thus, the models are estimated according to the training set, and the predictions in the test period are made by assuming that only MENA CORDEX is available. Then, MERRA-2 is estimated and compared with the original data.

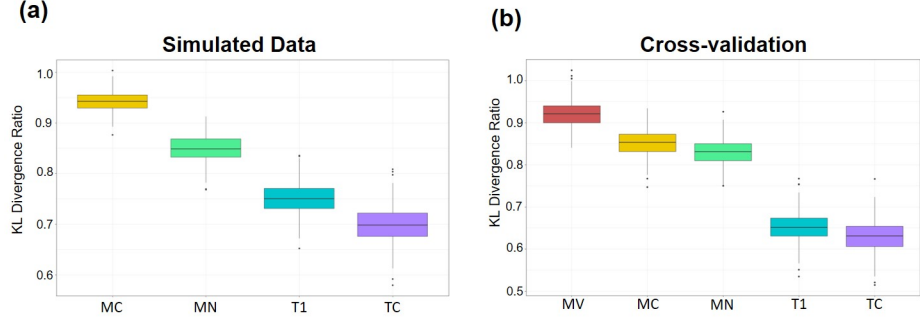


Figure 4: Boxplot of KL divergences between (a) MV and the MC, MN, T1 and TC method for the simulated data and (b) M and the MV, MC, MN, T1 and TC method for the estimated and actual MERRA-2 from 1993 to 2005. Each of the 1,000 elements of the boxplot represents an independent simulation in (a) and a random sub-sample of 300 locations in (b).

We compute the KL divergence (estimated and true MERRA-2 data in the testing set) ratio between the simple mean bias correction (M) and other approaches. The MV, MC, and MN approach result in ratios of 0.93, 0.88, and 0.81, respectively, indicating an increasingly faithful representation of MERRA-2 if the variance and covariance are estimated. Our proposed approach can further decrease the KL ratio to 0.58 and 0.51 for T1 and TC, respectively.

To assess the uncertainty in the KL ratio, for 1,000 times we sample 300 points (from the total $n = 614$ in the spatial domain) from the spatial domain, perform the correction methods, and estimate the KL ratio for each sample. Each boxplot in Figure 4(b) represents the KL ratio between M and the other approaches for each subsample. For MC, MN and T1 methods, we estimate the covariance function parameters for each sample. In the case of the transformation, we used the same parameters as for the full data set for computational convenience. For TC, we used k -means and a stratified sampling method

to select 50% of the locations in each cluster. Overall, the improvement in the proposed model is apparent throughout the subsamples, with an increasingly small KL divergence and with our proposed T1 and TC methods yielding the smallest divergence.

6 Application

We use the proposed approach to estimate how the daily revenue from the current optimal turbines build-out in Saudi Arabia will be impacted by a changing climate over the next few decades. In subsection 6.1 we describe our approach for extrapolating the predicted surface wind to hub height, whereas in subsection 6.2 we assess the final change in profits implied by the corrected data extrapolated at hub height.

6.1 Extrapolation to hub height

In Figure 5(a) the daily surface wind speed according to MERRA-2 is presented. This map indicates spatial patterns of potential interest for wind harvesting, especially in the north-west corner, which is a site of particular interest because of the ongoing project to build a self-sustainable city (NEOM, (12)). However, the surface wind does not necessarily represent the wind at higher altitudes. Indeed, the wind speed data from both MENA CORDEX and MERRA-2 are computed or observed at a reference height of 10 meters, whereas wind turbines normally operate at a height of 80-120 meters. Therefore, in order to assess the wind energy output, the surface wind speed must be extrapolated to the height at which wind turbines operate. There is a vast literature on extrapolating wind speed from surface to a height within the boundary layer, see (10) for a comprehensive

review. In the vast majority of studies, the power law is used:

$$W_O^{(F)}(\mathbf{s}_i, t_j, h_k) = W_O^{(F)}(\mathbf{s}_i, t_j, h_r) \left(\frac{h_k}{h_r} \right)^{\alpha_{i,j}} e^{\eta(\mathbf{s}_i, t_j)}, \quad (12)$$

$$\eta(\mathbf{s}_i, t_j) \sim \mathcal{N}(0, \sigma_i^2),$$

where h_k is the height to which we want to extrapolate and h_r is the height at which data are available (in our case is 10 meters). The α is the *shear coefficient* of the power law, and its value is assumed to change depending on local spatial properties such as surface roughness and thermal stability (i.e., the temperature gradient for the first layers in the boundary layer) (15). In the absence of any meteorological information, the standard approach is to assume that $\alpha_{ij} = 1/7$, which corresponds to a value observed on flat terrain under neutral atmospheric conditions (38; 42). Direct estimation of α_{ij} using MERRA-2 or MENA CORDEX is impossible, as direct estimation of the power law from (12) would require sufficient vertical wind levels below 100 meters, and neither data sets is designed for this level of accuracy near the surface. In this study, we rely instead on a high resolution WRF ensemble and select a run by adopting a planetary boundary layer parameterization, resolution and boundary conditions resulting in simulations closer to a few in-situ data available (14). The WRF simulation is specifically designed to capture the wind at a high resolution near the surface, and resolves the wind speed vertical profile at six levels, which are approximately equally spaced from the ground level to an altitude of 100 meters. Therefore, these data will be used to estimate α_{ij} and σ_i^2 in (12). Since we focus on daily data (neither MERRA-2 nor MENA CORDEX has hourly data) and a preliminary analysis (not shown) did not highlight temporal changes in the shear coefficient, $\alpha_{ij} = \alpha_i$ is estimated from the power law with a simple log regression.

The map of the estimated wind shear coefficients, along with their standard deviations and the coefficients of determination R^2 can be observed from Figure S12. The map of the estimates indicates a considerable spatial variability, with very small and even negative

values of the shear coefficient closely associated with the mountainous areas of the Hejaz region in the west. While slower wind at high altitudes is an unexpected (yet physically admissible) behavior within the boundary layer, it often occurs in areas exhibiting the smallest R^2 and the largest standard deviation, indicating that the power law (12) is likely not an appropriate model, as also indicated in many studies (15; 8). Since the installation of wind turbines is not cost effective in the rough terrains of Saudi Arabia (14), the model misspecification over these regions is not a major concern. Once the α_i are estimated, MERRA-2 data are then downscaled from the 50×50 km to the 6×6 km WRF resolution with ordinary kriging using another Matérn (5) covariance, and the wind speed at the desired hub height is computed. Finally, given the uncertainty associated with the determination of the shear coefficients, we performed 1,000 extrapolations for each site by simulating both the shear coefficient with its variability, as well as the random noise from the parameters estimated in (12).

Figure 5(b) shows the extrapolated average daily wind at 100 meters for MERRA-2 during 2025-2050. Besides being uniformly faster than wind at the surface, the spatial patterns are not drastically different from those in panel (a), as expected. Figure S13 shows the relative change of 100 meter wind against surface wind, and highlights how the increase in wind speed ranges from 60% to about 85%.

6.2 Assessing changes in future wind energy revenues

(14) showed that the most cost effective choice of turbines depends upon the site, because the construction and maintenance cost as well as the potential for harnessing the wind vary. Here, we use the same map of the most efficient turbines as indicated in Figure 5(a) of the aforementioned manuscript, and extrapolate the surface wind to the hub height of each turbine type. The wind speed is translated into energy through a turbine-specific power curve, which is a function that represents the ability of the turbine to translate the blade

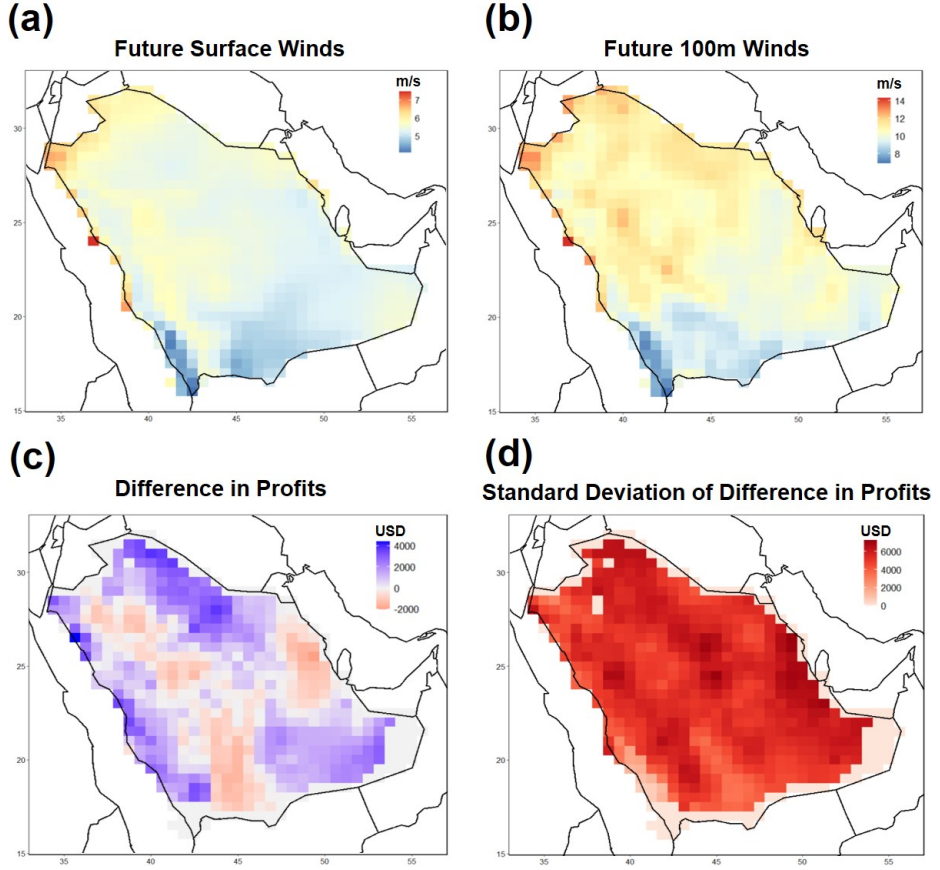


Figure 5: Maps of averaged daily wind speed at (a) the surface and (b) 100 meters from 2025 to 2050, and (c) average differences between the future and historical wind energy profits and their standard deviations (d).

movement into energy. Power curves are zero until a given wind speed, increase up to a maximum rated power and are constant for any stronger wind. The power curves for specific turbines are not available to the public domain, and in this study we used a proprietary database purchased from *The Wind Power* (www.thewindpower.net/about_en.php). The total energy output per cell can be calculated by multiplying the power for a single turbine with the total number of turbines, is dependent on the diameter of the rotor blade and has

to allow sufficient spacing among turbines to avoid local turbulence (wake effect), which would reduce the overall efficiency.

Finally, the wind power is translated into actual revenue using the current tariffs of the Saudi Electricity Company (www.se.com.sa/en-us/customers/Pages/TariffRates.aspx), which is approximately 5 US cents per kWh. The current estimate is likely to be sensibly overestimated because the associated direct and indirect costs were not accounted for. The difference in revenue, as implied by the changes between future and present wind, is presented in Figure 5(c). Overall, the map indicates increased revenues of up to approximately \$4,000 per day for the vast majority of the sites. Most importantly, the sites with increased future revenues are those located near the coasts, hence with more potential for wind harvesting, and especially the NEOM region in the north west. The regions towards the center of Saudi Arabia, including the neighborhoods of the capital Riyadh would incur a loss in revenue from changes in wind, if turbines were to be installed there, although it would not be as substantial as in the other areas. The uncertainty map is presented in Figure 5(d), and indicates large uncertainties in some areas, especially near the Persian Gulf. While these uncertainties are arguably large in some areas, they are a direct consequence of the considerable daily variability of the power law (12). The uncertainty in the use of the power law has been acknowledged (15; 8), even though it has not been frequently used with the goal of uncertainty quantification, but in relation to additional covariates such as temperature gradients and stability metrics, which cannot be determined in this study given the coarse vertical structures of MERRA-2 and MENA CORDEX.

While the aforementioned maps provide an overall estimation of the difference in profits across the country, the areas of highest interest are the ones where the installation of wind turbines would be the most cost-effective choice. Therefore, we estimate the difference in profits for the 75 wind farms locations identified in (14) to be the most promising sites. We add the difference in profits across the sites and we obtain a total increase in profit

of approximately \$273,000 and a standard deviation of \$15,000, hence lending additional support for the long-term profitability of the selected sites.

7 Conclusion

In this study, we have addressed the issue of resilience of Saudi Arabia’s current plan to diversify its energy portfolio with wind energy under changing climate conditions. The key element associated with this assessment is the estimation of future winds using reanalysis data. In order to provide that, we proposed a novel trans-Gaussian cluster-wise adjustment model based on minimizing the KL divergence between reanalysis and simulated data. Once the model was properly validated with a simulation study and with historical data, we estimated future winds from 2025 to 2050. These estimates were extrapolated to the turbine hub height using the output from high resolution numerical model simulations specifically designed to capture the vertical structure in the boundary layer. Finally, these estimates were translated into wind power and changes in revenue from future to present winds. Results show a sizable increase of approximately \$273,000 in daily revenues at the ideal construction sites, albeit with a standard deviation of \$15,000 due to the uncertainty propagated by the extrapolation of wind from the surface to hub height.

From a methodological perspective, our model generalized some of the most common approaches used for correcting spatial fields to the non-Gaussian case and proposed an inferential approach that could be scaled to considerably higher spatial resolutions for future data sets with 1) clustering of the trans-Gaussian transformation and 2) numerical approximation of the KL divergence with k nearest neighbors. The limitations of the current approach will likely become apparent if hourly or sub-hourly resolution were made available: in that case, the space-time interaction could not be reduced to a simple vector moving average model and would likely require nonseparable models, the application of

which would considerable increase the computational cost. Furthermore, high resolution wind data would 1) result in sparse wind such that a simple trans-Gaussian model could not capture, and a more involved latent Gaussian model would be required and 2) invalidate extrapolation with the power law, which available literature suggests to use only up to hourly resolution. This would prompt the development of more sophisticated nonparametric approaches such as neural networks (49).

From the applied perspective, even though extrapolation is widely acknowledged to be the most important source of uncertainty associated with the determination of wind energy from surface wind, this study did not account for other sources. First, MERRA-2 is only one of the available reanalysis data products, so further comparison with other products, such as the new ERA5 from the European Centre for Medium-Range Weather Forecasts (19), could be performed. Second, power curves have been obtained from proprietary data, but the raw data used to determine them are confidential, and would likely indicate some degree of uncertainty with respect to the determination of the said curve. Third, the translation of power into revenue is highly dependent upon policies and negotiations between the turbine operators and local authorities; therefore this may vary across different regions of Saudi Arabia. Future work will focus on better assessing these sources of uncertainty by engaging both industrial partners and policymakers, and discussing potential changes in the siting work conducted by (14) in lights of these new results.

Finally, we emphasize how the scope of this study could be generalized to any country with an emerging wind energy portfolio. Even though vertical extrapolation required a high resolution ensemble focused on Saudi Arabia and energy costs are expected to change across different countries, the core of our methodology involves only publicly available data and hence can be used to inform strategies for other Gulf countries and beyond. Furthermore, in lieu of new data from a high-resolution ensemble, the power law could be simplified to the case of neutral atmospheric stability and flat terrain, a simplifying assumption widely

accepted in wind power literature.

References

- [1] A. Azzalini and A. Capitanio. Distributions generated by perturbation of symmetry with emphasis on a multivariate skew t-distribution. *Journal of the Royal Statistical Society: Series B (Statistical Methodology)*, 65(2):367–389, 2003. doi: 10.1111/1467-9868.00391. URL <https://rss.onlinelibrary.wiley.com/doi/abs/10.1111/1467-9868.00391>.
- [2] S. Boltz, E. Debreuve, and M. Barlaud. knn-based high-dimensional kullback-leibler distance for tracking. In *Eighth International Workshop on Image Analysis for Multimedia Interactive Services (WIAMIS '07)*, pages 16–16, 2007.
- [3] British Petroleum. BP statistical review of world energy, 2020. www.bp.com/content/dam/bp/en/corporate/pdf/energy-economics/statistical-review/bp-stats-review-2018-full-report.pdf.
- [4] S. Castruccio, H. Ombao, and M. G. Genton. A scalable multi-resolution spatio-temporal model for brain activation and connectivity in fmri data. *Biometrics*, 74(3):823–833, 2018. doi: 10.1111/biom.12844.
- [5] L. Chen, S. C. Pryor, and D. Li. Assessing the performance of intergovernmental panel on climate change ar5 climate models in simulating and projecting wind speeds over china. *Journal of Geophysical Research: Atmospheres*, 117:D24102, 2012. doi: 10.1029/2012JD017533. URL <https://agupubs.onlinelibrary.wiley.com/doi/abs/10.1029/2012JD017533>.

- [6] W. Chen, S. Castruccio, M. G. Genton, and P. Crippa. Current and future estimates of wind energy potential over saudi arabia. *Journal of Geophysical Research: Atmospheres*, 123(12):6443–6459, 2018. doi: 10.1029/2017JD028212. URL <https://agupubs.onlinelibrary.wiley.com/doi/abs/10.1029/2017JD028212>.
- [7] W. Chen, S. Castruccio, and M. G. Genton. Assessing the risk of disruption of wind turbine operations in saudi arabia using bayesian spatial extremes. *Extremes*, 2021. doi: 10.1214/17-AOAS1105. in press.
- [8] P. Crippa, M. Alifa, D. Bolster, M. Genton, and S. Castruccio. A heteroskedastic time-varying model for improved hourly wind power forecasting. 2020. under review.
- [9] J. P. Dunne, J. G. John, E. Shevliakova, R. J. Stouffer, J. P. Krasting, S. L. Malshev, P. C. D. Milly, L. T. Sentman, A. J. Adcroft, W. Cooke, K. A. Dunne, S. M. Griffies, R. W. Hallberg, M. J. Harrison, H. Levy, A. T. Wittenberg, P. J. Phillips, and N. Zadeh. GFDL’s ESM2 global coupled climate–carbon Earth system models. Part II: carbon system formulation and baseline simulation characteristics. *Journal of Climate*, 26(7):2247–2267, 04 2013. ISSN 0894-8755. doi: 10.1175/JCLI-D-12-00150.1.
- [10] S. Emeis. *Wind Energy Meteorology - Second Edition*. Springer, NY, 04 2018. ISBN 978-3-319-72858-2. doi: 10.1007/978-3-319-72859-9.
- [11] R. Erdin, C. Frei, and H. R. Künsch. Data transformation and uncertainty in geostatistical combination of radar and rain gauges. *Journal of Hydrometeorology*, 13(4):1332–1346, 08 2012. ISSN 1525-755X. doi: 10.1175/JHM-D-11-096.1. URL <https://doi.org/10.1175/JHM-D-11-096.1>.
- [12] A. Farag. The story of neom city: Opportunities and challenges. In I. A. Attia S., Shafik Z., editor, *New Cities and Community Extensions in Egypt and the Middle East*, pages 35–49. Springer, Cham, Switzerland, 2019.

[13] R. Gelaro, W. McCarty, M. J. Suárez, R. Todling, A. Molod, L. Takacs, C. A. Randles, A. Darmenov, M. G. Bosilovich, R. Reichle, K. Wargan, L. Coy, R. Cullather, C. Draper, S. Akella, V. Buchard, A. Conaty, A. M. da Silva, W. Gu, G.-K. Kim, R. Koster, R. Lucchesi, D. Merkova, J. E. Nielsen, G. Partyka, S. Pawson, W. Putman, M. Riendecker, S. D. Schubert, M. Sienkiewicz, and B. Zhao. The Modern-Era Retrospective Analysis for Research and Applications, Version 2 (MERRA-2). *Journal of Climate*, 30(14):5419–5454, 06 2017. ISSN 0894-8755. doi: 10.1175/JCLI-D-16-0758.1. URL <https://doi.org/10.1175/JCLI-D-16-0758.1>.

[14] P. Giani, T. Felipe, M. G. Genton, S. Castruccio, and P. Crippa. Closing the gap between wind energy targets and implementation for emerging countries. *Applied Energy*, 269:115085, 2020. ISSN 0306-2619. doi: <https://doi.org/10.1016/j.apenergy.2020.115085>.

[15] G. Gualtieri. A comprehensive review on wind resource extrapolation models applied in wind energy. *Renewable and Sustainable Energy Reviews*, 102:215–233, 2019. doi: <https://doi.org/10.1016/j.rser.2018.12.015>.

[16] H. Hasanean and M. Almazroui. Rainfall: Features and variations over saudi arabia, a review. *Climate*, 3:578–626., 2015. doi: 10.1214/17-AOAS1105.

[17] E. Hawkins, T. M. Osborne, C. K. Ho, and A. J. Challinor. Calibration and bias correction of climate projections for crop modelling: An idealised case study over europe. *Agricultural and Forest Meteorology*, 170:19–31, 2013. ISSN 0168-1923. doi: <https://doi.org/10.1016/j.agrformet.2012.04.007>. Agricultural prediction using climate model ensembles.

[18] M. Hemer, K. McInnes, and R. Ranasinghe. Climate and variability bias adjustment of climate model-derived winds for a southeast aust-

tralian dynamical wave model. *Ocean Dynamics*, 62(1):87–104, 2012. ISSN 16167341. URL <http://search.ebscohost.com.proxy.library.nd.edu/login.aspx?direct=true&db=aph&AN=70162084&site=ehost-live>.

[19] H. Hersbach, B. Bell, P. Berrisford, S. Hirahara, A. Horányi, J. Muñoz-Sabater, J. Nicolas, C. Peubey, R. Radu, D. Schepers, A. Simmons, C. Soci, S. Abdalla, X. Abellán, G. Balsamo, P. Bechtold, G. Biavati, J. Bidlot, M. Bonavita, G. De Chiara, P. Dahlgren, D. Dee, M. Diamantakis, R. Dragani, J. Flemming, R. Forbes, M. Fuentes, A. Geer, L. Haimberger, S. Healy, R. J. Hogan, E. Hólm, M. Janisková, S. Keeley, P. Laloyaux, P. Lopez, C. Lupu, G. Radnoti, P. de Rosnay, I. Rozum, F. Vamborg, S. Villaume, and J.-N. Thépaut. The era5 global reanalysis. *Quarterly Journal of the Royal Meteorological Society*, 146(730):1999–2049, 2020. doi: 10.1002/qj.3803.

[20] D. Higdon. Space and space-time modeling using process convolutions. In C. W. Anderson, V. Barnett, P. C. Chatwin, and A. H. El-Shaarawi, editors, *Quantitative Methods for Current Environmental Issues*, pages 37–56, London, 2002. Springer London.

[21] C. K. Ho, D. B. Stephenson, M. Collins, C. A. T. Ferro, and S. J. Brown. Calibration strategies: a source of additional uncertainty in climate change projections. *Bulletin of the American Meteorological Society*, 93(1):21–26, 01 2012. doi: 10.1175/2011BAMS3110.1.

[22] International Renewable Energy Agency. Renewable energy statistics, 2018. <https://irena.org/publications/2018/Jul/Renewable-Energy-Statistics-2018>.

[23] International Renewable Energy Agency. Renewable energy market analysis: Gcc, 2019. <https://www.irena.org/publications/2019>.

[24] IPCC. Part a: Global and sectoral aspects. In *AR5 Climate Change 2014: Impacts, Adaptation, and Vulnerability*. Cambridge University Press., 2014.

[25] J. Jeong, S. Castruccio, P. Crippa, and M. G. Genton. Reducing storage of global wind ensembles with stochastic generators. *Annals of Applied Statistics*, 12(1):490–509, 03 2018. doi: 10.1214/17-AOAS1105.

[26] J. Jeong, Y. Yan, S. Castruccio, and M. G. Genton. A stochastic generator of global monthly wind energy with Tukey g-and-h autoregressive processes. *Statistica Sinica*, 29:1105–1126, 2019.

[27] K. B. Kim, H.-H. Kwon, and D. Han. Bias correction methods for regional climate model simulations considering the distributional parametric uncertainty underlying the observations. *Journal of Hydrology*, 530:568–579, 2015. ISSN 0022-1694. doi: <https://doi.org/10.1016/j.jhydrol.2015.10.015>. URL <http://www.sciencedirect.com/science/article/pii/S002216941500774X>.

[28] R. Kinley. Climate change after paris: from turning point to transformation. *Climate Policy*, 17(1):9–15, 2017. doi: 10.1080/14693062.2016.1191009.

[29] S. Kullback and R. A. Leibler. On information and sufficiency. *Annals of Mathematical Statistics*, 22(1):79–86, 03 1951. doi: 10.1214/aoms/1177729694.

[30] W. B. Leeds, E. J. Moyer, and M. L. Stein. Simulation of future climate under changing temporal covariance structures. *Advances in Statistical Climatology, Meteorology and Oceanography*, 1(1):1–14, 2015. doi: 10.5194/ascmo-1-1-2015. URL <https://ascmo.copernicus.org/articles/1/1/2015/>.

[31] D. Li, J. Feng, Z. Xu, B. Yin, H. Shi, and J. Qi. Statistical bias correction for simulated wind speeds over cordex-east asia. *Earth and Space Science*, 6(2):200–211,

2019. doi: 10.1029/2018EA000493. URL <https://agupubs.onlinelibrary.wiley.com/doi/abs/10.1029/2018EA000493>.

[32] NREP. Saudi arabia renewable energy targets and long term visibility, national renewable energy program, 2018.

[33] M. Nurunnabi. Transformation from an oil-based economy to a knowledge-based economy in saudi arabia: the direction of saudi vision 2030. *Journal of the Knowledge Economy*, 8(2):536–64, 2017.

[34] C. J. Paciorek and M. J. Schervish. Spatial modelling using a new class of nonstationary covariance functions. *Environmetrics*, 17(5):483–506, 2006. doi: 10.1002/env.785.

[35] M. B. Palacios and M. F. J. Steel. Non-gaussian bayesian geostatistical modeling. *Journal of the American Statistical Association*, 101(474):604–618, 2006. doi: 10.1198/016214505000001195.

[36] C. Piani and J. O. Haerter. Two dimensional bias correction of temperature and precipitation copulas in climate models. *Geophysical Research Letters*, 39:L20401, 2012. doi: 10.1029/2012GL053839.

[37] A. Poppick, D. J. McInerney, E. J. Moyer, and M. L. Stein. Temperatures in transient climates: Improved methods for simulations with evolving temporal covariances. *Annals of Applied Statistics*, 10(1):477–505, 03 2016. doi: 10.1214/16-AOAS903.

[38] S. Rehman, I. El-Amin, F. Ahmad, S. Shaahid, A. Al-Shehri, and J. Bakhshwain. Wind power resource assessment for rafha, saudi arabia. *Renewable and Sustainable Energy Reviews*, 11(5):937–950, 2007. ISSN 1364-0321. doi: <https://doi.org/10.1016/j.rser.2005.07.003>. URL <http://www.sciencedirect.com/science/article/pii/S1364032105000717>.

[39] REN21 Secretariat. Renewables 2018 - global status report, 2018. Paris, France.

[40] M. Risser and C. Calder. Local likelihood estimation for covariance functions with spatially-varying parameters: The convospa package for r. *Journal of Statistical Software, Articles*, 81(14):1–32, 2017. ISSN 1548-7660. doi: 10.18637/jss.v081.i14.

[41] M. Stein. *Interpolation of Spatial Data: Some Theory for Kriging*. Springer, NY, 1999.

[42] F. Tagle, S. Castruccio, P. Crippa, and M. G. Genton. A non-gaussian spatio-temporal model for daily wind speeds based on a multi-variate skew- t distribution. *Journal of Time Series Analysis*, 40(3):312–326, 2019. doi: 10.1111/jtsa.12437.

[43] F. Tagle, S. Castruccio, and M. G. Genton. A hierarchical bi-resolution spatial skew- t model. *Spatial Statistics*, 35:100398, 2020. ISSN 2211-6753. doi: <https://doi.org/10.1016/j.spasta.2019.100398>.

[44] F. Tagle, M. Genton, A. Yip, S. Mostamandi, G. Stenchikov, and S. Castruccio. A high-resolution bilevel skew- t stochastic generator for assessing saudi arabia’s wind energy resources (with discussion). *Environmetrics*, 31:e2628, 2020. doi: 10.1002/env.2628.

[45] K. E. Taylor, R. J. Stouffer, and G. A. Meehl. An overview of cmip5 and the experiment design. *Bulletin of the American Meteorological Society*, 93(4):485–498, 04 2012. ISSN 0003-0007. doi: 10.1175/BAMS-D-11-00094.1. URL <https://doi.org/10.1175/BAMS-D-11-00094.1>.

[46] C. Teutschbein and J. Seibert. Bias correction of regional climate model simulations for hydrological climate-change impact studies: Review and evaluation of different methods. *Journal of Hydrology*, 456-457:12–29, 2012. ISSN 0022-1694. doi: <https://doi.org/10.1016/j.jhydrol.2012.05.052>. URL <http://www.sciencedirect.com/science/article/pii/S0022169412004556>.

[47] UNFCCC. Intended nationally determined contributions: Kingdom of Saudi Arabia, 2020. www4.unfccc.int/sites/submissions/INDC/Published%20Documents/Saudi%20Arabia/1/KSA-INDCs%20English.pdf.

[48] D. P. van Vuuren, J. Edmonds, M. Kainuma, K. Riahi, A. Thomson, K. Hibbard, G. C. Hurtt, T. Kram, V. Krey, J.-F. Lamarque, T. Masui, M. Meinshausen, N. Nakicenovic, S. J. Smith, and S. K. Rose. The representative concentration pathways: an overview. *Climatic Change*, 109:5–31, 2011.

[49] D. Vassallo, R. Krishnamurthy, and H. J. S. Fernando. Decreasing wind speed extrapolation error via domain-specific feature extraction and selection. *Wind Energy Science*, 5(3):959–975, 2020. doi: 10.5194/wes-5-959-2020.

[50] M. Vrac and P. Friederichs. Multivariate—intervariable, spatial, and temporal—bias correction. *Journal of Climate*, 28(1):218–237, 12 2014. ISSN 0894-8755. doi: 10.1175/JCLI-D-14-00059.1. URL <https://doi.org/10.1175/JCLI-D-14-00059.1>.

[51] Q. Wang, S. R. Kulkarni, and S. Verdu. Divergence estimation for multidimensional densities via k -nearest neighbor distances. *IEEE Transactions on Information Theory*, 55(5):2392–2405, 2009.

[52] World Bank. Energy use (kg of oil equivalent per capita), 2020. <https://data.worldbank.org/indicator/EG.USE.PCAP.KG.OE>.

[53] I.-K. Yeo and R. A. Johnson. A new family of power transformations to improve normality or symmetry. *Biometrika*, 87(4):954–959, 2000.

[54] Q. Yuan, T. L. Thorarinsdottir, S. Beldring, W. K. Wong, S. Huang, and C.-Y. Xu. New approach for bias correction and stochastic downscaling of future projections for daily mean temperatures to a high-resolution grid. *Journal of Applied Meteorology*

and *Climatology*, 58(12):2617–2632, 12 2019. doi: 10.1175/JAMC-D-19-0086.1. URL <https://doi.org/10.1175/JAMC-D-19-0086.1>.